Earth's Future

RESEARCH ARTICLE
10.1029/2020EF001634

Detectability of Artificial Ocean Alkalinization and Stratospheric Aerosol Injection in MPI-ESM

Friederike Fröb[1], Sebastian Sonntag[1,2], Julia Pongratz[1,3], Hauke Schmidt[1], and Tatiana Ilyina[1]

[1]Max Planck Institute for Meteorology, Hamburg, Germany, [2]Climate Service Center Germany (GERICS), Helmholtz-Zentrum Geesthacht, Hamburg, Germany, [3]Department of Geography, Ludwig-Maximilians-Universität München, Munich, Germany

Key Points:
- Detectability is robust using regularized optimal fingerprinting and single-model estimates of internal variability
- Changes in the CO_2 system in seawater are detected earlier than the thermodynamic response to AOA but later in the case of SAI
- Local detectability depends on patterns of internal variability and physical, chemical, and radiative impacts of external forcing

Correspondence to:
F. Fröb,
friederike.froeb@mpimet.mpg.de

Citation:
Fröb, F., Sonntag, S., Pongratz, J., Schmidt, H., & Ilyina, T. (2020). Detectability of artificial ocean alkalinization and stratospheric aerosol injection in MPI-ESM. *Earth's Future*, *8*, e2020EF001634. https://doi.org/10.1029/2020EF001634

Received 22 MAY 2020
Accepted 2 OCT 2020
Accepted article online 14 OCT 2020

Correction added on 7 November 2020, after first online publication: Projekt Deal funding statement has been added.

©2020. The Authors.
Earth's Future published by Wiley Periodicals LLC on behalf of American Geophysical Union

This is an open access article under the terms of the Creative Commons Attribution-NonCommercial-NoDerivs License, which permits use and distribution in any medium, provided the original work is properly cited, the use is non-commercial and no modifications or adaptations are made.

Abstract To monitor the success of carbon dioxide removal (CDR) or solar radiation management (SRM) that offset anthropogenic climate change, the forced response to any external forcing is required to be detectable against internal variability. Thus far, only the detectability of SRM has been examined using both a stationary and nonstationary detection and attribution method. Here, the spatiotemporal detectability of the forced response to artificial ocean alkalinization (AOA) and stratospheric aerosol injection (SAI) as exemplary methods for CDR and SRM, respectively, is compared in Max Planck Institute Earth System Model (MPI-ESM) experiments using regularized optimal fingerprinting and single-model estimates of internal variability, while working under a stationary or nonstationary null hypothesis. Although both experiments are forced by emissions according to the Representative Concentration Pathway 8.5 (RCP8.5) and target the climate of the RCP4.5 scenario using AOA or SAI, detection timescales reflect the fundamentally different forcing agents. Moreover, detectability timescales are sensitive to the choice of null hypothesis. Globally, changes in the CO_2 system in seawater are detected earlier than the response in temperature to AOA but later in the case of SAI. Locally, the detection time scales depend on the physical, chemical, and radiative impacts of CDR and SRM forcing on the climate system, as well as patterns of internal variability, which is highlighted for oceanic heat and carbon storage.

1. Introduction

The Parties to the United Nations Framework Convention on Climate Change (UNFCCC) agreed to drastically reduce their CO_2 emissions in order to limit warming by the end of this century to 2 °C above preindustrial levels (p. 2, UNFCCC, 2015). However, curbing CO_2 emissions alone may no longer be sufficient (Rogelj et al., 2016), and carbon dioxide removal strategies (CDR) and solar radiation management (SRM) may need to be deployed in order to meet these temperature targets (Fuss et al., 2014; Lawrence et al., 2018; Royal Society, 2009). Before any of these options become part of a portfolio of strategies to address the challenges posed by anthropogenic climate change, potential side effects and risks need thorough evaluation. For this, it is crucial to ensure detectability of CDR or SRM signals in order to attribute any observed changes to a particular cause. Only then can the success of CDR or SRM be monitored, and in case unpredicted side effects occur, liability claims can then be made (Pfrommer et al., 2019).

CDR differs fundamentally from SRM (Royal Society, 2009; Vaughan & Lenton, 2012). CDR strategies include all anthropogenic activities that remove atmospheric CO_2 and durably store it in either long-term reservoirs or products (IPCC, 2018). Hence, not only would the temperature response to anthropogenic CO_2 emissions be tackled (Caldeira et al., 2013; Tavoni & Socolow, 2013) but also the problem of ocean acidification would likewise be addressed (Doney et al., 2009). SRM strategies on the other hand modify the shortwave radiative budget of the atmosphere (IPCC, 2018) such that a larger amount of incoming solar radiation is reflected back to space and the temperature response to CO_2 emissions is damped (Crutzen, 2006; Irvine et al., 2016). In this study, an exemplary measure for each strategy is employed: artificial ocean alkalinization (AOA) for CDR and stratospheric aerosol injection (SAI) for SRM. AOA accelerates the uptake and storage of atmospheric CO_2 in the ocean that would occur naturally on time scales of ~100–200 ka through the chemical weathering of silicate rocks (Hartmann et al., 2013). SAI, in the form of particles or their precursor gases such as sulfur dioxide analogous to a volcanic eruption, could reduce the rate of global

warming through enhancing the albedo of the stratospheric aerosol layer (Irvine et al., 2016). Depending on the deployment scale, both in space and time, for either AOA or SAI, the resulting signals may be potentially obscured by the natural variability of the climate system, which complicates detectability.

Detection is first and foremost a statistical term: Any observed change in a climate variable or in a process is detected if the signal is significantly different from natural internal variability (Bindoff et al., 2013). A given signal can only be confidently attributed to a certain cause, if first, the change is consistent with the expected response to a forcing or driver and second, no other explanation for the observed change can be found (e.g., Allen & Tett, 1999; Hasselmann, 1993; Hegerl et al., 1997). Classical detection and attribution methods, that is, optimal fingerprinting methods, use climate model output to quantify the expected responses to external forcing and internal variability in order to evaluate evidence found in observational data (Hegerl & Zwiers, 2011). The underlying assumption that the statistics of the climate is stationary in the absence of external forcing may no longer hold with ongoing emissions of greenhouse gases as well as additional forcing agents such as CDR or SRM (Bürger & Cubasch, 2015; Lo et al., 2016). The impact of either SRM or CDR on the mean state of the climate system and its dynamics remains to be tested, particularly on regional scales, where signal-to-noise ratios of externally forced changes are generally decreased (Stott, 2003).

Thus far, only the detectability of SRM temperature and precipitation signals has been examined using a classical optimal fingerprinting approach (Lo et al., 2016, 2018) and a nonstationary detection method (Bürger & Cubasch, 2015; Lo et al., 2016), for global (Bürger & Cubasch, 2015; Lo et al., 2016) and regional perspectives (Lo et al., 2018). All three previous studies are based on climate model data from the Geoengineering Model Intercomparison Project (GeoMIP; Kravitz et al., 2011) and used simulations of the multimodel Coupled Model Intercomparison Project Phase 5 (CMIP5; Taylor et al., 2012) to evaluate internal variability, despite individual models not being independent from each other and equal treatment of all models may induce biases (Knutti et al., 2013). Moreover, intermodel differences in the simulated SRM response patterns are potentially large and may lead to nonphysical detection and attribution results (Ribes & Terray 2013; Ribes et al., 2017).

In this study, only single-model estimates of the externally forced response based on experiments run with the state-of-the-art, Max Planck Institute Earth System Model (MPI-ESM; González & Ilyina, 2016; González et al., 2018; Sonntag et al., 2018) are considered. Moreover, single-model estimates of internal variability provided by the Max Planck Institute Grand Ensemble (MPI-GE; Maher et al., 2019) are used to avoid potential biases that may be related to the sampling uncertainty of internal variability in the CMIP5 database. The detectability of forced responses to AOA and SAI in global mean near-surface air temperature is evaluated and compared using both a classical optimal fingerprinting approach and a nonstationary detection method. While SAI targets only temperature, AOA directly impacts the global carbon cycle; therefore, surface ocean hydrogen ion concentration ($[H^+]$) signals as a measure of pH are evaluated as well. pH itself is a logarithmic parameter and therefore not suitable for the regularized optimal fingerprinting approach. Beyond the SRM-only studies by Bürger and Cubasch (2015) and (Lo et al., 2016, 2018), here, the detectability of global mean AOA and SAI signals and their local patterns are discussed. Most detection studies focus on temperature only; here, the discussion is extended using the example of AOA and SAI-driven carbon inventory and ocean heat content changes and their detectability.

2. Methodology

2.1. Model Description

The model experiments were run using the Max Planck Institute Earth System Model (MPI-ESM, version 1.0.02p1) in the low-resolution (LR) configuration as in CMIP5 (Giorgetta et al., 2013). MPI-ESM includes components of the ocean (MPIOM; Jungclaus et al., 2013), atmosphere (ECHAM6; Stevens et al., 2013), land surface and terrestrial biosphere (JSBACH; Reick et al., 2013), and marine biogeochemistry (HAMOCC5; Ilyina et al., 2013). The fully coupled carbon cycle mode of MPI-ESM allows to calculate atmospheric CO_2 prognostically in response to prescribed CO_2 emissions. The CMIP5 experiments include a preindustrial control simulation (ESM-CNTL, 1,000 years) and three realizations of each of the emission-driven historical experiment (1850–2005) and the emission-driven Representative Concentration Pathway 8.5 (RCP8.5) scenario run (2006-2100). A detailed discussion on MPI-ESM evaluation can be found in Giorgetta et al. (2013) and references therein.

The MPI-GE (version MPI-ESM 1.1.00p2) allows to estimate model internal variability in a transient scenario (Maher et al., 2019). Compared to MPI-ESM used in CMIP5, MPI-GE has a slightly different ocean component and a different version of ECHAM6, while using the CMIP5 configuration of HAMOCC5 and JSBACH, including the soil carbon model YASSO (Goll et al., 2015) and a five-layer soil hydrology scheme (Hagemann S. & Stacke, 2015). Additionally, cloud feedback parameters were adjusted, which lead to an equilibrium climate sensitivity that is lowered from 3.4 K in CMIP5 to 2.8 K in MPI-GE (Maher et al., 2019). Here, the concentration-driven 100-member ensemble for the historical simulations (1850–2005) and RCP8.5 scenario run (2006–2100) are used. The MPI-GE runs are used for the nonstationary detection method (Bürger & Cubasch, 2015), assuming that the similarities between model versions are large, the differences in internal variability between concentration-driven MPI-GE and emission-driven MPI-ESM runs are minor, the differences in internal variability despite the slightly different climate sensitivity are minor, and these differences are very likely smaller compared to a multimodel CMIP5 ensemble.

2.2. AOA and SAI Scenario

Both AOA and SAI experiments (González & Ilyina, 2016; González et al., 2018; Sonntag et al., 2018) use the solar irradiance, land use transitions, aerosols, and atmospheric concentrations of greenhouse gases according to RCP8.5, while through the application of AOA and SAI, the climate of the RCP4.5 scenario is targeted. RCP8.5 is the only no-mitigation CMIP5 scenario and therefore allows comparison to AOA or SAI as large-scale intervention options. The RCP4.5 target climate is significantly different to the RCP8.5 base climate state. AOA and SAI experiments are initialized from the emission-driven historical CMIP5 experiment (Giorgetta et al., 2013) in 2006 and are run until 2100. Both experiments consist of an ensemble of three members.

In the AOA scenario, atmospheric CO_2 concentrations are designed to follow the RCP4.5 trajectory, while the CO_2 emissions increase according to RCP8.5 (González & Ilyina, 2016; González et al., 2018). The cumulative emissions of the RCP8.5 scenario are 910 GtC larger than those of the RCP4.5 scenario. This excess amount of carbon can be taken up by the ocean through enhancing the oceanic CO_2 buffer capacity. Thereby, the entire ocean is turned into a sink for atmospheric CO_2, even areas that act as a source of carbon to the atmosphere in the modern ocean (González & Ilyina, 2016). This can be achieved by adding alkalinity every time step to the first ocean model level, that is, to the upper 12 m of the ocean, as soon as the difference between actual and RCP4.5 atmospheric CO_2 concentration is larger than 1% which occurs in 2018. In total, 114 Pmol of alkalinity are added until 2100.

In the SAI scenario, the radiative forcing is designed to follow the RCP4.5 trajectory, while the CO_2 emissions increase according to RCP8.5 (Sonntag et al., 2018). As there is no explicit calculation of aerosol concentrations in ECHAM6, the aerosol optical properties are prescribed every time step starting 2006 in order to mimic the radiative effects of enhancing stratospheric aerosols by injecting sulfur (Niemeier et al., 2013; Niemeier & Timmreck, 2015). By 2100, almost 20 Mt S $year^{-1}$ is assumed.

2.3. Regularized Optimal Fingerprinting

The detection of a climate signal can be claimed, if that signal is no longer within the bounds of internal variability. If the same signal is consistent with the expected response to different combinations of external forcings, the signal can be attributed to its cause (Bindoff et al., 2013). Many detection and attribution studies are based on the optimal fingerprinting approach that was introduced by Allen and Tett (1999), Allen and Stott (2003), Hasselmann (1993), and Hegerl et al. (1997). Essentially, in this linear regression technique, an observed signal is regressed onto the expected response to external forcing. Assuming that the response to several external forcings is additive, the following linear regression model applies:

$$\mathbf{y} = \sum_{i=1}^{f} \beta_i \mathbf{X}_i + \varepsilon \tag{1}$$

Here, $\mathbf{y}$ is the observed signal, $\mathbf{X}_i$ is the response to the ith of f external forcings, β_i is an unknown scaling factor, and ε denotes the internal climate variability. In order to estimate the confidence intervals of the linear regression model in Equation 1, the covariance matrix of the internal climate variability needs to be evaluated, assuming that ε is a Gaussian random variable. Particularly, for data sets with a large spatial or spatiotemporal size this is challenging. Therefore, here a regularized estimate of the covariance matrix is used, which avoids underestimation of high-order eigenvalues (Ribes et al., 2009, 2013).

While in the ordinary least squares approach (Allen & Tett, 1999), $\mathbf{X}_i$ is assumed to be perfectly known, in the total least square approach (Allen & Stott, 2003), $\mathbf{X}_i$ is unknown. The total least square approach is used here, where the ensemble mean, $\tilde{\mathbf{X}}_i$, is provided by the climate model simulation: $\tilde{\mathbf{X}}_i = \mathbf{X}_i + \varepsilon_{X_i}$. Here, ε_{X_i} represents internal climate variability and, as such, can be written as $\mathrm{Cov}(\varepsilon_{X_i}) = \frac{1}{n}\mathrm{Cov}(\varepsilon)$, while n represents the number of ensemble members used to calculate $\tilde{\mathbf{X}}_i$.

2.4. Defining the Null Hypothesis

The classical statistical model for optimal fingerprinting techniques assumes a stationary, unperturbed state of the climate such that the null hypothesis is derived from observed normals (Bürger & Cubasch, 2015). In this case internal variability is based on the preindustrial, emission-driven control run of MPI-ESM, while both the responses to RCP8.5 forcing and to additional forcing of the large-scale climate intervention (LSI), that is, AOA or SAI, have to be taken into account to assess detectability:

$$\begin{aligned} \tilde{y}_{\mathrm{obs,LSI}} &= \tilde{\beta}_1 \tilde{\mathbf{X}}^*_{\mathrm{LSI}^*} + \tilde{\beta}_2 \tilde{\mathbf{X}}_{\mathrm{RCP8.5}} + \varepsilon \\ &= \tilde{\beta}_1 (\tilde{\mathbf{X}}_{\mathrm{LSI}} + \tilde{\mathbf{X}}_{\mathrm{RCP8.5}}) + \tilde{\beta}_2 \tilde{\mathbf{X}}_{\mathrm{RCP8.5}} + \varepsilon \\ &= (\tilde{\beta}_1 + \tilde{\beta}_2) \tilde{\mathbf{X}}_{\mathrm{RCP8.5}} + \tilde{\beta}_1 \tilde{\mathbf{X}}_{\mathrm{LSI}} + \varepsilon \end{aligned} \tag{2}$$

No observations are available for the future signals; therefore, one ensemble member of the SAI or AOA scenario is used as a pseudo-observation $\tilde{y}_{\mathrm{obs,LSI}}$. The simulated response patterns to the external forcing, the so called fingerprints, are defined as the mean over the remaining two ensemble members of the SAI and AOA experiment ($\tilde{\mathbf{X}}_{\mathrm{LSI}}$), respectively, and the mean over the three ensemble members of the RCP8.5 scenario ($\tilde{\mathbf{X}}_{\mathrm{RCP8.5}}$). The results may depend on which of the three ensemble members has been assigned as pseudo-observation (see Appendix A1).

Note that the response of the LSI signal is not independent of the forced response of the RCP8.5 scenario as no AOA-only or SAI-only experiments are available. Therefore, the calculated scaling factor needs to be corrected (Equation 2 and Lo et al., 2016). Before regularized optimal fingerprinting is applied to calculate detectability, signal anomalies are estimated with respect to the 1991–2005 year mean period prior to the deployment of the large-scale climate intervention measure. The anomaly of the preindustrial control simulation is estimated by removing the 1,000-year mean state in order to have a zero-mean control climate (Hasselmann, 1993).

Following the line of argumentation by Bürger and Cubasch (2015), the climate evolution over the 21st century is per definition nonstationary. The long-term gradual warming as a consequence of the increasing emission of greenhouse gases introduces uncertainty as the future climate sensitivity is unknown. The grand ensemble MPI-GE-LR allows to adjust the null hypothesis accordingly. The 100-member RCP8.5 scenario run is used to evaluate the internal climate variability under forcing over the course of the 21st century. In this case, the assumed additivity of the response of external forcings is fully exploited. Here, the null hypothesis is formulated in a perfect model or at least a near-perfect model framework as two slightly different models, that is, MPI-GE and MPI-ESM are used, such that only the LSI response pattern remains in the statistical model:

$$\tilde{y}_{\mathrm{obs,\ LSI}} = \tilde{\beta}_{\mathrm{LSI}} \tilde{\mathbf{X}}_{\mathrm{LSI}} + \varepsilon \tag{3}$$

Note that due to the different climate sensitivity in MPI-ESM and MPI-GE and due to likely different response patterns, the anomalous signals cannot be estimated by removing the forced trend, that is, the 100-member mean (Maher et al., 2019). Instead, the anomaly of the AOA and SAI scenario is estimated by removing a 3-year running mean of the RCP8.5 run, that is, the forced trend over the three ensemble members of MPI-ESM. The filtering becomes necessary in order to avoid contamination of the observation with the fingerprint signal and vice versa. The estimates of the forced response of the MPI-ESM RCP8.5 run could be improved and recovered using dynamical adjustment techniques (Deser et al., 2016; Sippel et al., 2019), which, however, goes beyond the scope of this study.

Prior to the application of regularized optimal fingerprinting, all data are temporally smoothed using a causal, 10-year trend-based filter in order to reduce interannual variability (Bürger & Cubasch, 2015; Lo et al., 2016). The scaling factors β are estimated over time in order to evaluate the time of detection of signals due to the large-scale climate intervention. Note that despite not all signals being equally noisy, the same temporal filter was used for different variables.

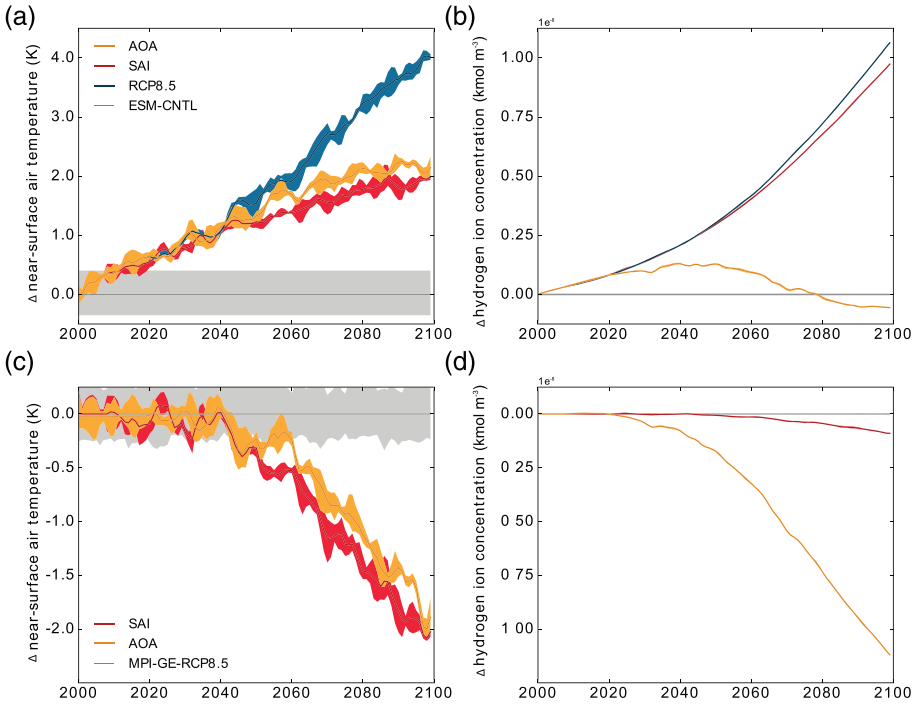

Figure 1. The anomalies of global, annual, 10-year trend-based filtered mean over three ensemble members for surface temperature (panels a, c) and hydrogen ion concentration (panels b, d) for RCP8.5 (blue), AOA (red), and SAI (orange) that serve as input for the optimal fingerprinting tool. Panels a and b show signals relative to the 1991–2005 mean to illustrate the stationary null hypothesis using a 1,000-year mean of ESM-CNTL (gray). Panels c and d show signals by removing the forced trend using a 100-member mean of MPI-GE, RCP8.5 (gray) to illustrate the nonstationary null hypothesis. The shaded areas illustrate the spread over 3 members, 100-members or 1,000 years, respectively.

2.5. Hypothesis Testing

Finally, the approach of Monte Carlo simulations introduced by Ribes et al. (2013) is applied to evaluate the consistency of the estimated global mean residuals in Equation 1 with internal climate variability. The residual consistency test fails when the variability of the residual in the observed signal is larger than the expected 5–95% range of internal variability from ESM-CNTL or MPI-GE or if the expected response patterns are incorrect (Ribes et al., 2013). Note that the grid pointwise Monte Carlo analysis is too costly to run; instead, residual consistency is estimated following Allen and Tett (1999) and Allen and Stott (2003). Due to small differences between the two residual consistency checks, local detectability results are shown at 10% significance levels.

The p value serves as criterion to either accept the null hypothesis, that is, "$\beta = 0$," or reject the null hypothesis, that is, "$\beta > 0$," at the 5% significance level for global signals and at the 10% significance level for local signals. Then, detection is the point in time after which the lower confidence interval of β_{SAI} or β_{AOA} or β_{RCP}, that is, the 5% (or 10%) significance level, is permanently larger than zero. That means, that there may be periods of time before, where the signal appears detectable, but becomes undetectable again over the course of the century. If "$\beta = 1$" can also not be rejected, attribution can be claimed; however, the focus within this study lies on the detectability.

3. Spatiotemporal Detectability of AOA and SAI

3.1. Global Signals

The time of detection allows to quantitatively compare CDR with SRM, illustrated for global and annual mean AOA and SAI near-surface air temperature and surface ocean hydrogen ion concentration ($[H^+]$) as a measure of pH signals over the 2005–2100 period under the stationary and nonstationary control climate. The chosen pointer variables show different magnitudes of change and levels of noise in the response patterns; therefore, regularized optimal fingerprinting can be well tested using different statistical models.

The signal anomalies that serve as input are slightly different for the two null hypotheses: Assuming a stationary control climate, anomalies are designed with respect to the 1991–2005 period (Figures 1a and 1b), while working under the assumption of a nonstationary control climate, the forced RCP8.5 trend is removed (Figures 1c and 1d).

Compared to the RCP8.5 experiment, both SAI and AOA lead to reduction in near-surface air temperature starting in the 2040s, and the reduction strongly increases until the end of the century (Figures 1a and 1c). The small offset by 2100 in the mean temperature signal between the AOA and SAI experiment is a consequence of a slightly different non-CO_2 greenhouse gas forcing, aerosol forcing, and effects of land use transitions (Modak et al., 2016; Sonntag et al., 2018). The tight relationship between atmospheric CO_2 and the CO_2 system in seawater leads to the smooth response of the H^+ concentration in the surface ocean to increasing atmospheric CO_2 levels over the course of the century (Figures 1b and 1d). The small reduction in atmospheric CO_2 in the SAI experiment due to a temperature-driven enhancement of terrestrial and oceanic carbon sinks (Sonntag et al., 2018) translates to a small reduction in surface ocean H^+ concentration (Figures 1b and 1d, red line), while in the AOA experiment, the increased oceanic buffer capacity mitigates the strong ocean acidification as in the RCP8.5 scenario and even produces pre-2000 global mean H^+ concentration signals by the end of the 21st century (González & Ilyina, 2016).

While Sonntag et al. (2018) and González and Ilyina (2016) analyzed and compared the magnitude of AOA and SAI signals, regularized optimal fingerprinting allows to quantify the point in time, at which these signals are detectable and no longer consistent with internal variability. The time series in Figure 2 show the evolution of the scaling factors calculated for the AOA and SAI experiments between 2006 and 2100 for surface temperature (first and third row panels) and hydrogen ion concentration (second and fourth row panels), assuming a stationary control climate (left and center rows, β_{SAI} or β_{AOA} and β_{RCP}) and a nonstationary control climate (right row, β_{SAI} or β_{AOA} only). The gray shaded area illustrates the failed residual consistency check (see section 2.5).

Assuming a stationary control climate, the global temperature response to SAI can be detected in 2066, while the response to AOA can be only detected roughly 10 years later, in 2075. Assuming nonstationarity, detection can be claimed earlier, that is, approximately in 2046 for SAI and 2051 for AOA. In all experiments, SAI is designed to balance all anthropogenic forcings and AOA only the CO_2 forcing (Sonntag et al., 2018). Therefore, the signal-to-noise ratio is slightly higher for temperature response to SAI than to AOA, which is reflected in β_{SAI} and β_{AOA}. As opposed to the GeoMIP data used by Bürger and Cubasch (2015) and Lo et al. (2016), the experiments here are designed to follow the RCP4.5 trajectory, but the temperature difference between RCP8.5 and RCP4.5 is relatively small until midcentury. The response patterns in temperature to the AOA or SAI forcing and the RCP8.5 forcing are therefore almost colinear until 2050, which complicates detectability as the corresponding signal-to-noise ratios are low. The evolution of the scaling factor β between 2006 and 2100 is accordingly noisy, particularly when assuming a stationary control climate. Detecting small anomalies close to zero toward the beginning of the century is challenging, because the linear regressions fail more easily.

In contrast, H^+ concentration signals are already detectable within the first 5 to 10 years after the deployment of AOA in 2018, with little difference between the stationary and nonstationary null hypothesis. The input of alkalinity over time directly affects the CO_2 system in seawater with a robust signal-to-noise ratio; therefore, changes in H^+ concentration due to AOA are detectable before 2025. For SAI, changes in the H^+ concentration can be detected 15 years earlier in the middle of the 21st century if the nonstationary null hypothesis is assumed compared to the stationary control climate. In principle, H^+ concentration is not a variable of choice to detect the impact of SAI mitigation; however, SAI indirectly affects atmospheric CO_2 concentration via an enhanced terrestrial carbon sink (Sonntag et al., 2018), which in turn imprints on surface ocean H^+ concentration.

The residual consistency test compares the estimated residuals of the statistical model with the modeled internal climate variability (section 2.5; Ribes et al., 2013). In general, close to the time of detection the regressions become significant at the 95% confidence level, that is, p values are smaller than 0.05. If a nonstationary control state is assumed, detection can not only be claimed earlier but is also more robust. Although Lo et al. (2016) find similar results in their comparison study, they dismiss the use of the nonstationary control case for their purpose.

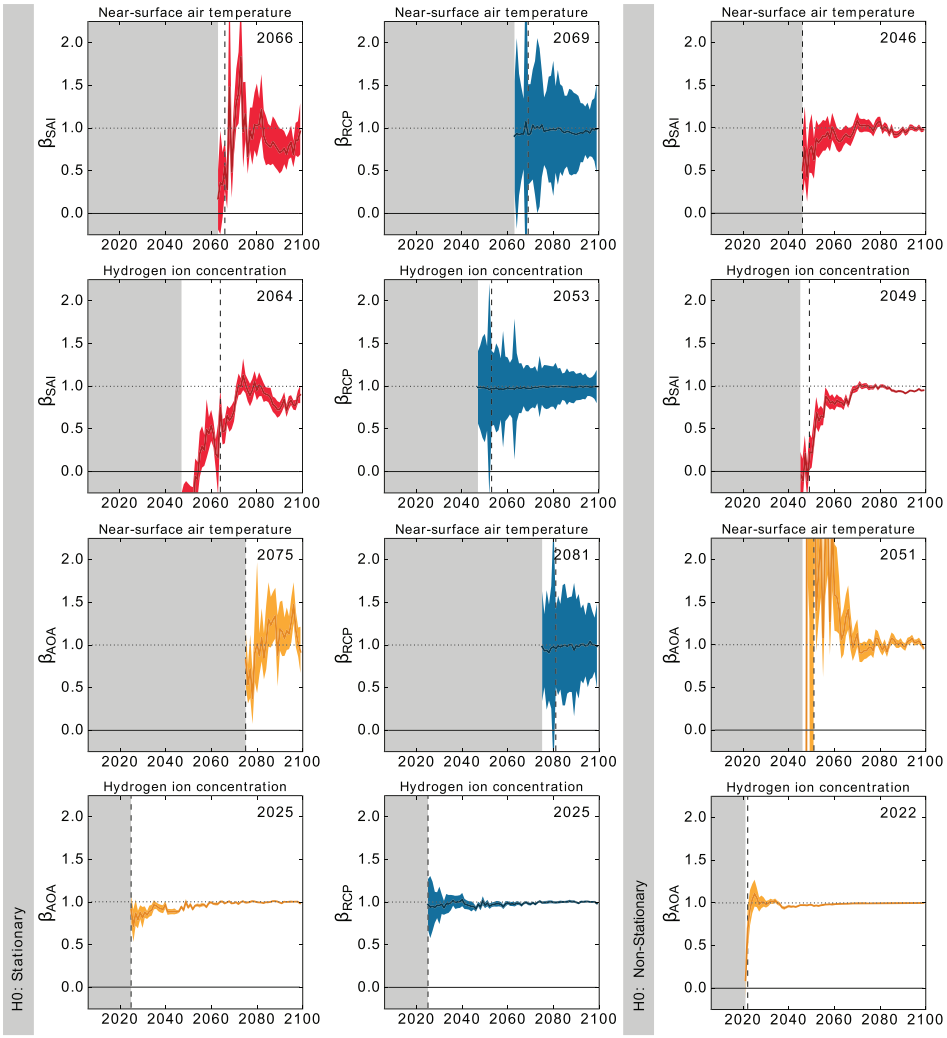

Figure 2. Detection and attribution for global mean-annual mean SAI and AOA signals. Scaling factors for surface temperature (first and third row panels) and hydrogen ion concentration (second and fourth row panels) under the stationary assumption (left and center panels) and under the nonstationary assumption (right panels). The dashed line indicates the time of detection, that is, the lower confidence interval is larger than 0 (year indicated in top right corner). The failed residual consistency check is highlighted by the gray shaded area, that is, p values larger than 0.05.

3.2. Local Signals

Global mean AOA and SAI signals are expected to be detected earlier then local signals, because patterns of internal variability that may compete on local scales are averaged, leading to reduced noise on global scales (Schlunegger et al., 2019). Despite potentially high local internal variability, local detection of the forced responses to AOA and SAI can eventually be claimed if signal-to-noise ratios become high enough. This is tested by processing the data as before, but instead of using global mean AOA and SAI signals, regularized optimal fingerprinting was applied at every grid point. In order to reduce noise, local signals are spatially averaged over all adjacent grid points for surface air temperature and H^+ concentration, assuming the non-stationary control climate first as it has yielded more robust results for global scale estimates (Figure 3) and assuming the stationary control climate (Figure 4).

By design, the overall AOA forcing counterbalances only the RCP8.5 CO_2 forcing, while SAI balances all anthropogenic RCP8.5 forcing. Therefore, the magnitude of SAI-driven cooling signals is larger than the AOA-driven signals, globally and locally. As the resulting signal-to-noise ratios remain low well throughout the century, the AOA signals are consequently detected later in the 2060s and beyond. For SAI, earlier

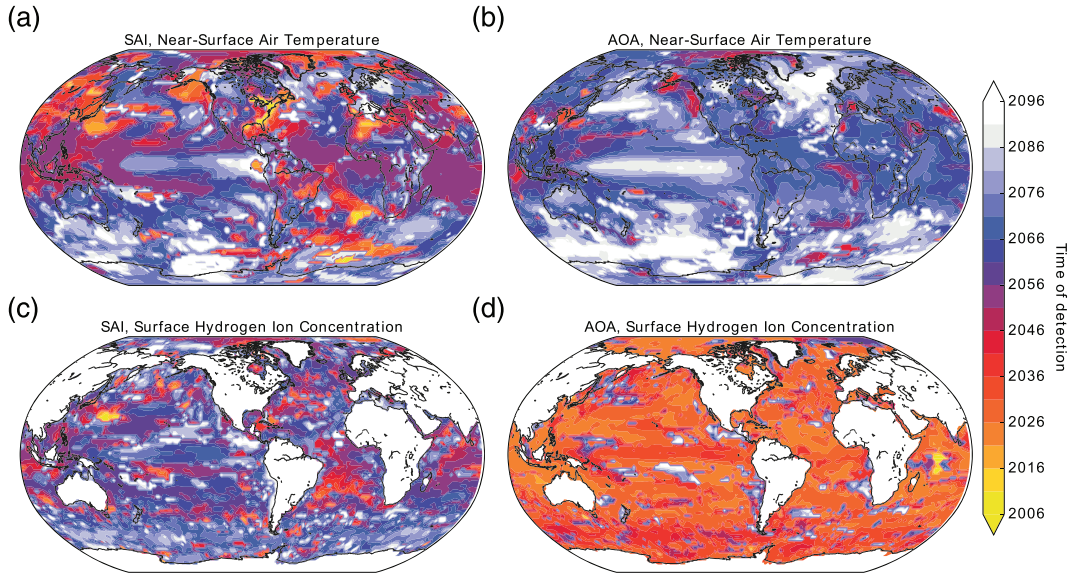

Figure 3. Local detectability for temperature (panels a, b) and hydrogen ion concentration (panels c, d) for SAI (panels a, c) and AOA (panels b, d) simulations. Regularized optimal fingerprinting was applied to every grid point assuming a nonstationary control climate.

detectability in the 2030s and 2040s is claimed in the low latitudes, in the Northern Hemispheric high latitudes as well as in a small area over the Atlantic sector in the Southern Ocean. In general, the fundamentally different radiative impact of either external forcing can be detected within the framework of regularized optimal fingerprinting (Figures 3a and 3b). The magnitude of internal variability on local scales shows minor differences between MPI-ESM and MPI-GE; that is, the variability patterns are slightly different (see Appendix A3). Working under the transient null hypothesis, this may lead to a small range in estimates of the uncertainty of the scaling factors within this only "near-perfect" model framework. Note that areas are hatched in the global maps presented in Figure 3 where the variability of the residuals, that is, the component of the observations not explained by the forcings, is larger than expected from the 10–90% range of internal variability of MPI-GE.

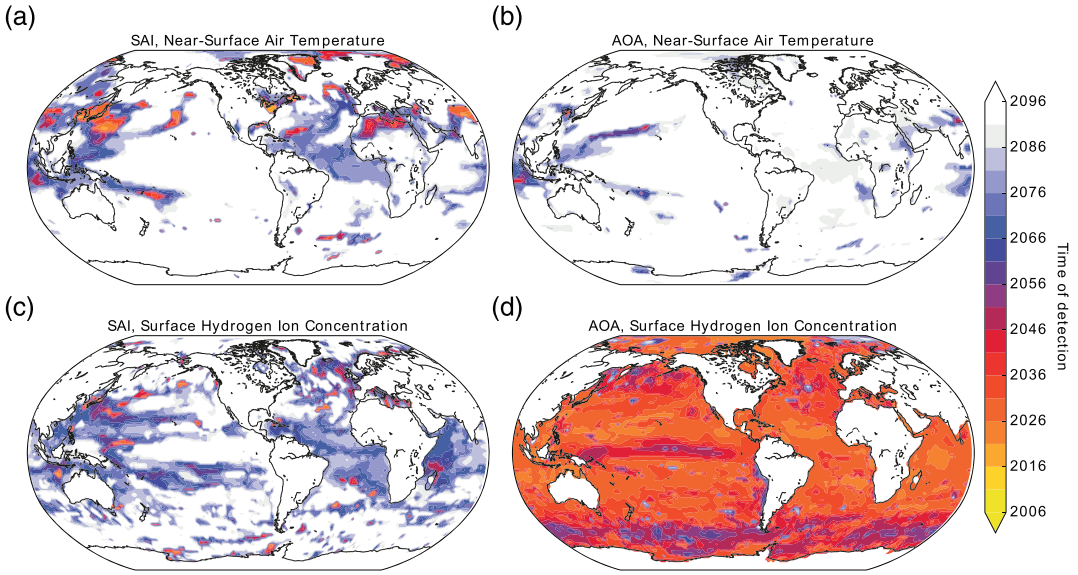

Figure 4. Local detectability for temperature (panels a, b) and hydrogen ion concentration (panels c, d) for SAI (panels a, c) and AOA (panels b, d) simulations. Regularized optimal fingerprinting was applied to every grid point assuming a stationary control climate.

On local scales, the cooling due to both SAI and AOA is more pronounced on land than on the ocean, more pronounced in the Arctic than at low latitudes, and low in the Southern Ocean (Sonntag et al., 2018). Although the time of detection for global mean near-surface air temperature is almost the same, locally, the spatial distribution of SAI and AOA time of detection resembles known variability patterns that emerge due to both atmospheric and oceanic processes (Figures 3a and 3b). Areas, in which temperatures deviate more frequently from long-term annual means, that is, that show large nonseasonal variability, are the Southern Ocean and Antarctica, the North Atlantic as well as northern Europe, and the North Pacific as well the upwelling zones along the equatorial Pacific (see Appendix A3 and e.g., Deser et al., 2010). These prominent features of temperature variability may be associated with modes of atmospheric circulation variability such as the Southern Annual Mode, the Atlantic Multidecadal Oscillation, the Pacific Decadal Oscillation, and coupled ocean-atmosphere interactions such as the El Niño–Southern Oscillation (Deser et al., 2010). In contrast to that, comparably low variability occurs across the tropical ocean basins with the exception of the tropical Eastern Pacific, where signal-to-noise ratios can be maximized earlier such that detectability can be claimed sooner as well.

Although the magnitude of variability patterns of H^+ concentration is less pronounced than temperature patterns, they may also be associated with circulation-driven variations in surface dissolved inorganic carbon associated with modes of atmospheric circulation variability (Lovenduski et al., 2015). The internal variability of surface ocean CO_2 system is spatially more heterogeneous, because equilibration timescales of surface waters to increasing atmospheric CO_2 affect local air-sea CO_2 fluxes (Friedrich et al., 2012). As signals associated with SAI in atmospheric CO_2 are small, changes in H^+ concentration in the climate system can be detected at the earliest in the middle of the 21st century (Figure 3c). Detection is claimed even later in the 2070s in the upwelling zones along coastal Peru and Chile, the Arctic Ocean, and large areas in the Southern Ocean. The changes in H^+ concentration are not only driven by the uptake of atmospheric CO_2; temperature signals contribute as well to H^+ concentration signals, which is why similarities to the SAI near-surface air temperature patterns emerge. In contrast to SAI signals, the direct intervention in the surface ocean CO_2 system can be detected within the first 10 to 20 years of AOA deployment in 2018 (Figure 3d). The signal-to-noise ratio is accordingly high, and the local time of detection of H^+ concentration shows a close to uniform distribution, as alkalinity is added every time step in every grid box homogeneously.

Assuming a stationary null hypothesis, the role of individual forcings that contributes to the observed change in a climate signal should be separated by simultaneously regressing two fingerprints onto the observations. The importance of the choice of null hypothesis is illustrated in all maps of Figure 4, which shows the same as Figure 3 but assuming a stationary control climate state. For near-surface air temperature, both SAI and AOA signals (Figures 4a and 4b) are scarcely detectable on a local scale this century. Only a few areas in the low latitudes stand out with detection times of around 60 years after the deployment of SAI. For the H^+ concentration, SAI signals in the low latitudes may be detected; however, the spatial detectability pattern is highly heterogeneous (Figure 4c). Despite the small signal in surface ocean H^+ concentration in response to SAI forcing, detectability can be claimed earlier than for near-surface temperature, because of higher signal-to-noise ratios. Only the H^+ concentration signals in the AOA experiment can be detected (Figure 4d) and an almost similar pattern emerges as in the map shown in Figure 3d.

The shift in the detectability pattern between the two null hypotheses, which is clearly visible for H^+ concentration signals in the AOA experiment (Figure 5), indicates that the assumption of additive responses to forcing may fail on local scales (Meehl et al., 2003). The choice of null hypothesis has little effect on the time of detection in large areas of the ocean, and the difference in the time of detection is smaller than 5 years. However, H^+ concentration signals in areas prone to higher internal variability such as the tropical Pacific, the Southern Ocean, upwelling close to the coast of Peru and Chile, and the northern high latitudes (see Appendix A3) are detected up to 30 years later assuming a stationary control climate, despite independence between forcings being assumed.

The failure for detection using a stationary background in a "perfect" model framework climate state indicates that the response to the RCP8.5 forcing and the AOA or SAI forcing, respectively, lacks detail in space and time. The responses to AOA or SAI and RCP8.5 forcing are therefore either indistinguishable, or the magnitudes of the signals are too small on local scales. This could be overcome by taking information from adjacent grid boxes into account to improve the filtering of data. The failure to detect engineered forcing

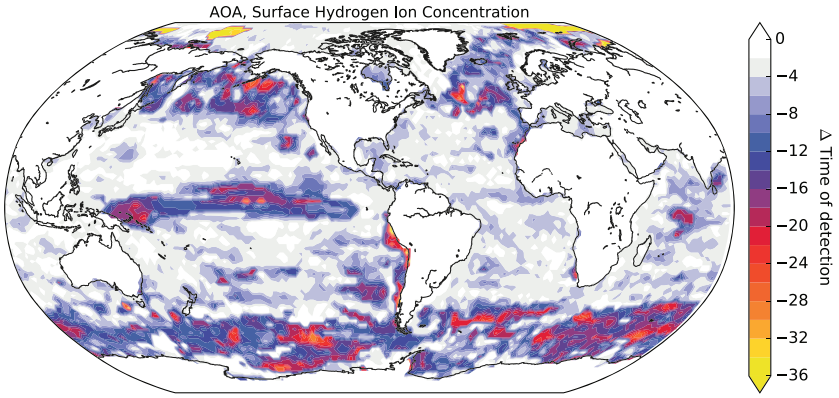

Figure 5. Difference in local detectability for hydrogen ion concentration between a nonstationary and stationary control climate.

should, therefore, not be interpreted as that no influence exists through SAI or AOA locally but rather that the forced responses to either forcing are not detectable above the internal variability.

4. Implications for Local Carbon Inventory and Heat Content Changes

For the purpose of detecting changes of the climate response to cumulative carbon emissions and changes thereof through AOA or SAI deployment, it might be more meaningful to assess the oceanic storage of anthropogenic carbon and heat. The oceans play a crucial role in climate change mitigation as they constitute an important sink for both anthropogenic heat and carbon albeit with large interannual to decadal variability (Frölicher et al., 2015; Thomas et al., 2018). The responses to SAI-driven changes in the shortwave radiative forcing and AOA-driven longwave radiative forcing should not only be separable to the RCP8.5 forcing in observed temperature trends or changes in the surface ocean CO_2 system. Instead, the regularized optimal fingerprinting may also be applied to carbon inventory changes, that is, the integrated column inventory of dissolved inorganic carbon, and to ocean heat content changes, that is, the integrated heat content between the surface ocean and 69-m depth. The analysis of nontemperature variables might increase confidence in the detection and attribution results.

The signal anomalies between the AOA and SAI scenario, respectively, and the RCP8.5 scenario by the end of the 21st century illustrate the strong carbon storage due to AOA as opposed to negligible storage due to SAI (Figures 6a and 6b). The largest AOA-driven carbon inventory changes are observed in the North Atlantic, the subtropical gyres, and in the Arctic, while the upwelling areas in the Atlantic and Pacific, the ENSO region in the tropical Pacific and Southern Ocean, are associated with little carbon inventory changes. Compared to the organized carbon inventory pattern, both scenarios lead to a reduced uptake of heat in the upper ocean over the course of the century with similar but finer patterns (Figures 6c and 6d). The largest reduction in upper ocean heat content occurs in the North Atlantic current, the Kuroshio current, the Antarctic Circumpolar current, and and the tropical Pacific. SAI leads to a slightly larger reduction in upper ocean heat content than AOA.

Assuming a nonstationary control climate state, the time of detection is shown in all maps of Figure 7. As expected, SAI has negligible impact on storage of carbon, which is why no detectability can be claimed in the open ocean. Despite the close to uniform detectability pattern for the surface ocean CO_2 system in response to the homogeneous application of alkalinity, the detectability pattern of carbon inventory changes resembles the large-scale ocean circulation pattern. Earliest detection is claimed in areas subject to strong convection that transfer carbon-enriched surface water masses to the deep ocean, that is, the North Atlantic, where signals were strongest as well. Large areas in the Southern Hemispheric midlatitudes show early detectability as well, due to larger signal-to-noise ratios. Despite high levels of carbon inventory changes due to AOA in the subtropical Pacific, high internal variability obscures detectability.

The slightly larger magnitude of heat storage due to SAI than AOA results in earlier detectability of these signals; however, the patterns are generally more structured compared to carbon. The SAI-driven changes in ocean heat content are detected earliest in the Northern Pacific and the tropical Atlantic and Indian

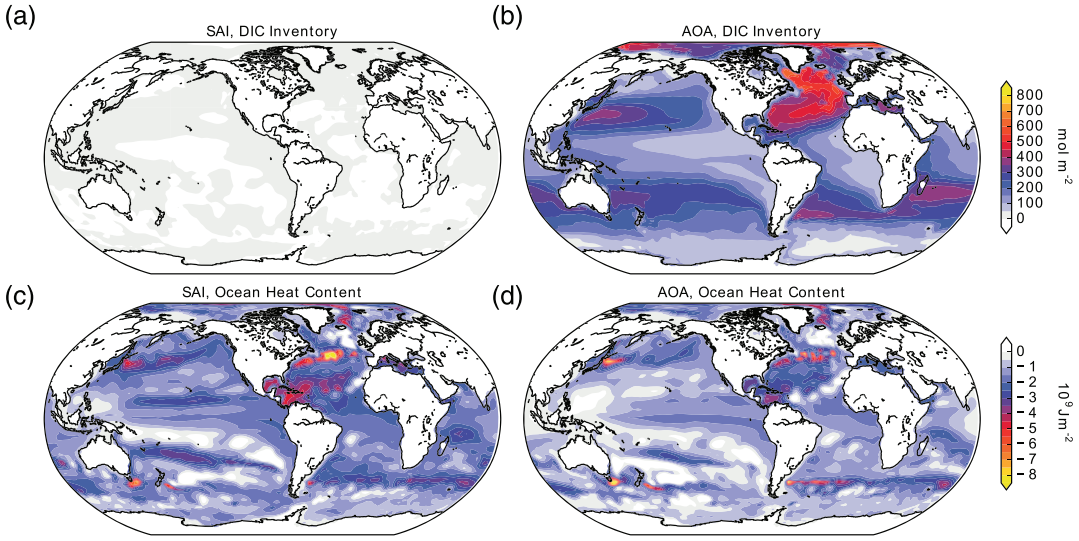

Figure 6. Ensemble mean change in depth-integrated dissolved inorganic carbon (panels a, b) and upper ocean heat content (panels c, d) for SAI (panels a, c) and AOA (panels b, d) simulations between the ensemble mean of the RCP8.5 scenario for the mean period 2090–2099.

Oceans. Except for the Indian Ocean feature, a similar pattern emerges for the AOA scenario, but later, with large areas with no detection at all prior to 2100. For both AOA and SAI, detectability is not exclusively claimed in areas with the strongest signals of heat invasion, which indicates higher internal variability in, for example, the subtropical North Atlantic. Over the historic period, variability in global carbon content using the suite of CMIP5 models stems mainly from Southern Ocean circulation changes (Frölicher et al., 2015; Thomas et al., 2018), while variability in ocean heat content is primarily driven by variability in the southern midlatitudes and tropical regions (Thomas et al., 2018). This leads to anticorrelated global heat and carbon content variability. Here, SAI and AOA forcing impact the timescales of heat and carbon uptake kinetics, air-sea equilibria, and atmospheric boundary conditions that lead to distinct patterns in magnitude and variability of oceanic heat and carbon storage. Regularized optimal fingerprinting can therefore be used to distinguish the mechanisms that are impacted by the deployment of SAI or AOA with statistical confidence.

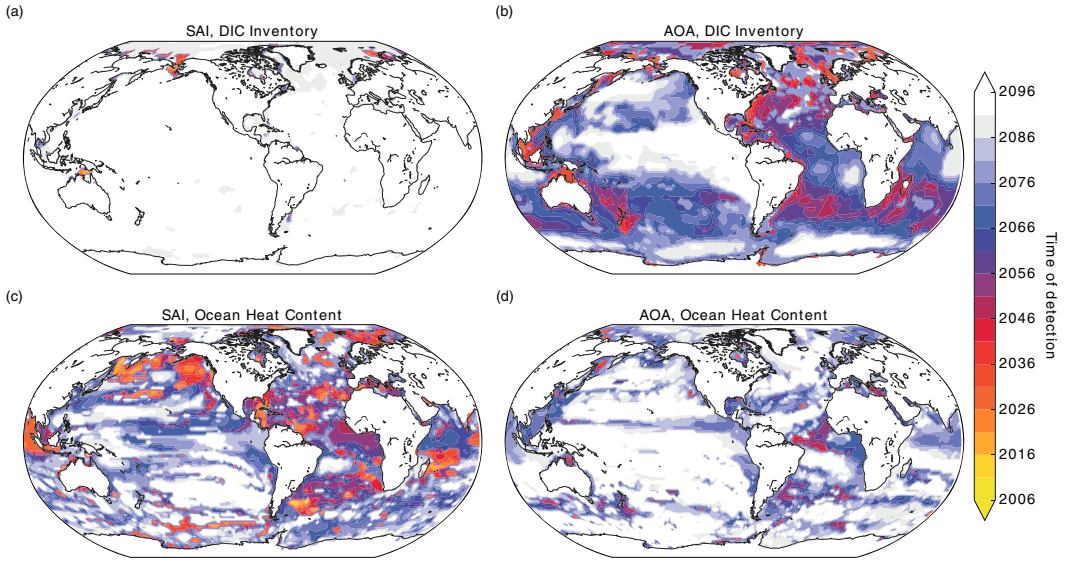

Figure 7. Local detectability for dissolved inorganic carbon (DIC) inventory (panels a, b) and upper ocean heat content (panels c, d) for SAI (panels a, c) and AOA (panels b, d) simulations. Regularized optimal fingerprinting was applied to every grid point assuming a nonstationary control climate.

5. Robustness of Results

In this study, the detectability results rely on the MPI-ESM simulations. Using a different Earth System Model will yield similar detectability time scales for global variables, if the simulated responses to anthropogenic forcing and SAI or AOA forcing are similar (Hegerl & Zwiers, 2011). On local scales, different detectability patterns will likely emerge due to different spatial patterns of the response to external forcing in different models, distinct from patterns of internal variability. Using single-model estimates of observation, fingerprints and internal variability is an advantage in this study, because the discrepancies between simulated response patterns of different models do not need to be taken into account (Ribes et al., 2017). Using multimodel estimates will likely result in longer detection time scales, as shown in Bürger and Cubasch (2015) for imperfect models with imperfect initial conditions. In general, detection and attribution studies that rely on multimodel assessments can be more confident that their fingerprints better represent the "true" response to forcing (Hegerl & Zwiers, 2011). If either SAI or AOA would ever be deployed, multimodel ensembles should be used to robustly detect climate change mitigation.

Beyond the structural uncertainty associated with MPI-ESM itself, the choice of the high-CO_2 emission scenario RCP8.5 as a background climate state and RCP4.5 as a target climate also affects the detectability results. If a lower and likely more plausible emission scenario (Hausfather & Peters, 2020) would have served as a base line, the temperature response to either SAI or AOA would likely be detected even later due to a lower magnitude of signal responses. The rapid response of hydrogen ion concentration to AOA prior to the divergence of the RCP4.5 and RCP8.5 scenarios midcentury suggests that here detection time scale is scenario independent. Therefore, SAI detection is limited, even in the highly idealized framework of this study, whereas AOA detection, if identified in carbon system parameters, is less sensitive to the deployment scale.

The robustness of the results depends further on the preprocessing of the data, the construction of the response to forcing, that is, the fingerprints, and the uncertainty of the internal variability estimates. As pointed out by Ribes et al. (2013), with regularized optimal fingerprinting, the choice of appropriate spatial and temporal filtering remains problematic as different filter lengths suppress or enhance different patterns of variability. Depending on the parameter, the detectability time scale changes using different filter length scales as different frequency components are smoothed over time (see Appendix A2), which remains to be tested locally. Applying a more refined spatial filtering, that is, taking information from larger regions into account, could improve signal detail in space and time. Then uncertainty for local detectability may be reduced, especially while working under a stationary null hypothesis.

Using only two ensemble members, as done in this study, to construct the fingerprints might not be sufficient to remove all remnants of internal variability (Hegerl & Zwiers, 2011). Particularly for near-surface temperature, where signal-to-noise ratios are low, especially on local scales, uncertainty in the fingerprints might be large (see Appendix A1). However, the total least squares approach shows only little sensitivity to small ensembles (Allen & Stott, 2003); therefore, increasing the ensemble size might not improve detectability estimates.

With ongoing climate change, internal variability will likely change, which has been shown in many studies for, for example, daily summer temperatures over Europe (Fischer & Schär, 2008), Atlantic Meridional Overturning Circulation (Drijfhout et al., 2008), precipitation (Pendergrass et al., 2017), surface-air temperature as well as sea ice volume and area (Olonscheck & Notz, 2017). Already now, internal variability is the dominant source of uncertainty in climate projections of potential ocean ecosystem stressors at global and regional scales for the next few decades (Frölicher et al., 2016). While with the advent of large ensembles, the potential change in internal variability due to greenhouse gas forcing can be better quantified, the impact of climate engineering on modes of internal variability remains largely unclear, especially for any CDR strategy. The deployment of SRM perturbs the Earth's energy balance, atmospheric dynamics, and hydrological cycling and thereby affects the local response of heat waves and soil moisture extreme events (Dagon & Schrag, 2017) but has been shown to have little impact on El Niño–Southern Oscillation frequency (Gabriel & Robock, 2015). In terms of detectability, potential changes in internal variability introduce additional uncertainty, especially on local scales. Therefore, depending on the parameter, estimated detection and attribution timescales may be underestimated or overestimated.

6. Conclusions

The fundamentally different forcing mechanisms complicate any comparative assessment of SRM and CDR strategies (Oschlies et al., 2017; Sonntag et al., 2018; Zürn & Schäfer, 2013). In this study, the scenario design allows to compare the detectability of the effects of SAI and AOA as exemplary measures for SRM and CDR after deployment in 2006. Globally, signals in near-surface air temperature can be detected 5 years earlier, that is, in 2046, in the SAI experiment compared to the AOA experiment. While the direct intervention of AOA in the CO_2 system in seawater is detectable within the first years after its deployment, that is, before 2025, the response in atmospheric CO_2 to SAI is indirect, and as such, detectability of SAI-driven changes in H^+ concentration signals is claimed in the second half of the 21st century. Locally, the response in temperature and the CO_2 system in seawater as well as heat and inorganic carbon inventories to both AOA and SAI have distinct detectability patterns. High internal variability impedes detectability, particularly if signal-to-noise ratios are low.

In general, detection can be claimed earlier and the results are more robust while working with a transient background climate state instead of a stationary null hypothesis. For example, the temperature response to SAI is detected in 2066 working with a stationary null hypothesis, which is 20 years later than working with a nonstationary null hypothesis. Particularly on local scales are the response patterns to AOA or SAI and RCP8.5 forcing too similar or too small and therefore indistinguishable. Additionally, the assumed additivity of signals may no longer be valid, as shown with the example of hydrogen ion concentration. Such nonlinear behavior may limit the detectability of individual responses to single forcing agents. Still, constructing climate normals by taking the modeled warming trend due to greenhouse gases into account allows a realistic application of regularized optimal fingerprinting.

Within the framework of this study, the response to external forcing is by design well known and not subject to large uncertainty. However, if actually deployed, feedback mechanisms may amplify or dampen the response patterns to either AOA and SAI. Moreover, the climate impacts of well-mixed greenhouse gases are less uncertain than those of aerosols and other short-lived climate forcers (e.g., Zhao et al., 2019), because of complex aerosol-cloud interactions. While regularized optimal fingerprinting may actually be used to detect the individual response patterns to fundamentally different forcing agents such as CDR and SRM, additional uncertainty is introduced through the combination of observed and modeled climate data.

Depending on detectability patterns that result from grid pointwise regularized optimal fingerprinting, monitoring systems could be designed to allow for control the success of SAI or AOA locally. These observation time series need to be at least as long as the detection timescale and probably longer in areas prone to large internal variability. However, the deployment of a single SRM or CDR measure such as SAI or AOA to offset anthropogenic climate change on a global scale is not very likely, particularly as individual approaches may lead to unintended side effects. In fact, implementation of either SAI or AOA on the scale suggested in this study is currently not technically feasible (González & Ilyina, 2016; Sonntag et al., 2018). The implementation of a combination of a number of different SRM or CDR measures on smaller scales is far more likely in order to meet the global temperature target. However, this will limit the detectability of individual responses to single measures, particularly if signals are small or response patterns are similar or local variability is high. Therefore, nontemperature variables that show distinct response patterns to SRM or CDR measures should be analyzed as well in order to increase confidence in the detection and attribution results.

Appendix A

A1. Sensitivity of Detection Time Scale to Choice of Ensemble Member

Throughout the manuscript, the same ensemble member was assigned to be the pseudo-observation, while the mean over the remaining two ensemble members of the engineered experiment was used to represent the response pattern to the forcing. Uncertainty in the estimate of the response pattern to the forcing that stems from internal variability decreases with increasing ensemble size (Hegerl & Zwiers, 2011). Figure A1 shows the time of detection for different ensemble members chosen as pseudo-observation for SAI and AOA and near-surface air temperature and hydrogen ion concentration. The choice of ensemble member has minor influence on the timescale of detection, except for the SAI-driven hydrogen ion concentration. Here, detectability can be claimed significantly earlier if the second ensemble member is assigned as pseudo-observation. Including more ensemble members could potentially reduce the uncertainty associated

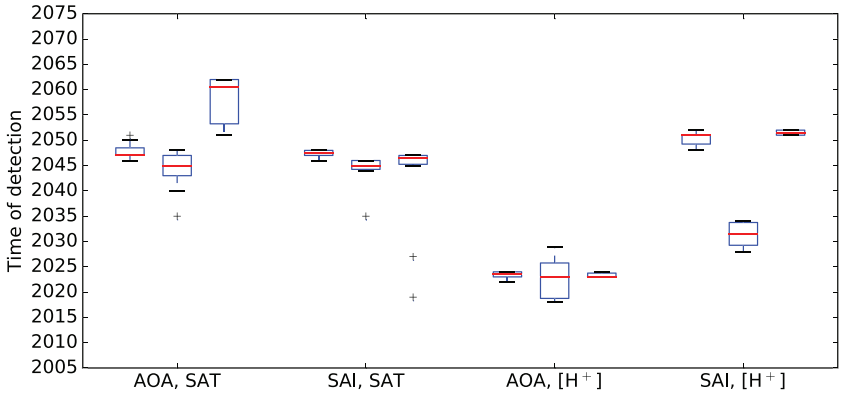

Figure A1. Sensitivity of detection timescale to choice of first, second, or third ensemble member as pseudo-observation. Distribution over window size of the filter between 5 and 15 years for AOA or SAI and near-surface air temperature (SAT) or hydrogen ion concentration ([H^+]).

with the choice of ensemble member. However, each member represents a potential realization of future climate that may include strong decadal trends that impact detectability independent of ensemble size.

A2. Sensitivity of Detection Time Scale to Choice of Filter

The optimal reduction of spatial and temporal dimension of the data before ROF may be used remains challenging (Ribes et al., 2013) as different filtering techniques may enhance or suppress different frequency components over time. Particularly assuming a nonstationary control climate state, the performance of a trend-based filter exceeds the one of a moving-average filter as no temporal phase shift occurs (Bürger & Cubasch, 2015). According to Lo et al. (2016), the choice of filter is crucial and determines the timescale of detectability, independent of the underlying null hypothesis. Both studies do not explicitly explore different window sizes of the filter and lengths of the base period but acknowledge that they might be of importance. Here, the time of detection is evaluated for global mean hydrogen ion concentration signals (Figure A2) and near-surface air temperature (Figure A3). One year is added stepwise in the length of the base period, that is, the time prior to the deployment of AOA or SAI, that is used as learning period (Ribes et al., 2013), and in case of the stationary control climate, to calculate signal anomalies. The window size of the filter ranges

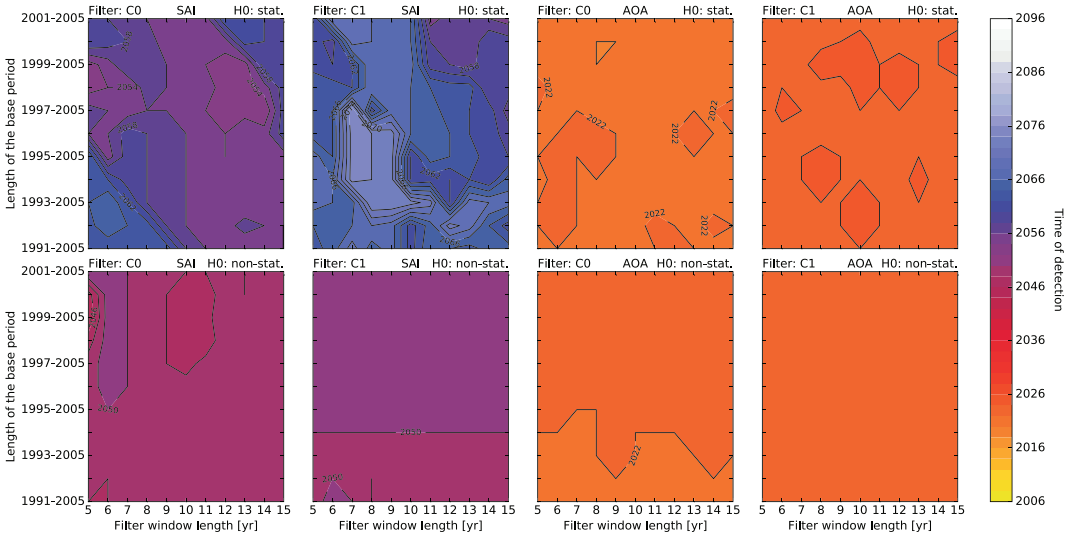

Figure A2. Sensitivity of detection timescale to choice of filter, size of filter window, and length of base period for hydrogen ion concentration signals in the SAI (left four panels) and AOA experiment (right four panels). Following the notation of Bürger and Cubasch (2015) and Lo et al. (2016), C0 stands for moving average filter and C1 for the trend-based filter. Both stationary (upper panels) and nonstationary null hypotheses (lower panels) are evaluated.

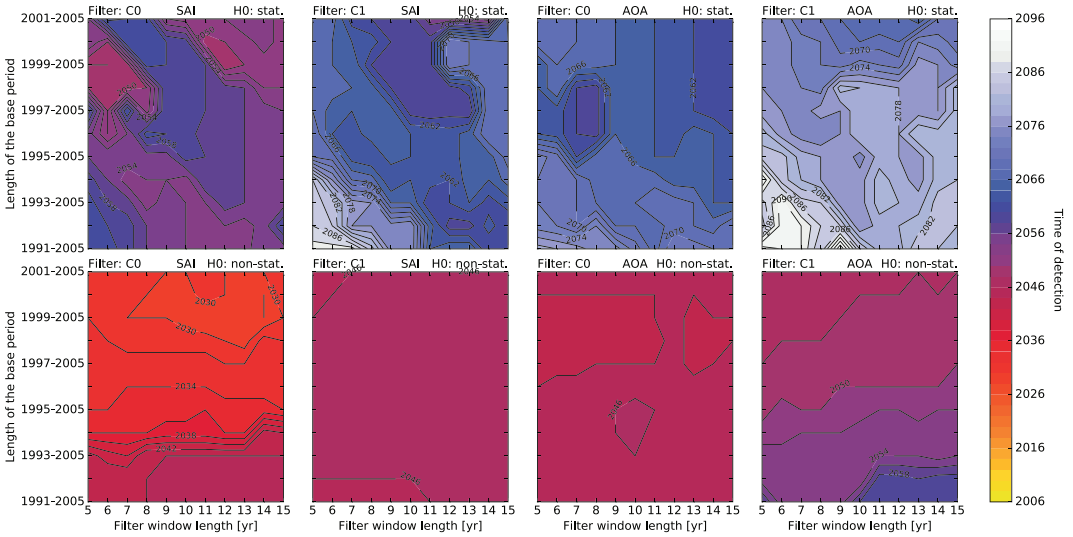

Figure A3. Same as Figure A2 but for near-surface air temperature signals.

between 5 and 15 years, that is, from a 5-year to a 15-year moving average filter or a 5- to 15-year trend-based filter.

Depending on variable and magnitude of the signal the choice of filter, both the length of the base period and size of the filter window can impact detectability. In general, the time of detection is more sensitive to the length of the base period, that is, the time prior to the deployment of AOA or SAI that is used as a learning period than the length of the filter window. The trend-based filter is less sensitive to the choice of length of the base period and filter window length than the moving average filter. The nonstationary null hypothesis yields more robust results than assuming a stationary control climate state. If signals are large enough, that is, for H^+ concentration in the AOA experiment, the time of detection is independent of the choice of filter or null hypothesis.

A3. Patterns of Annual Variability of the Control Climate States

In section 4, the patterns of internal variability of MPI-GE and ESM-CNTL are recognized in the maps of local detection timescale for both AOA and SAI. Figure A4 shows the mean standard deviation of anomalies

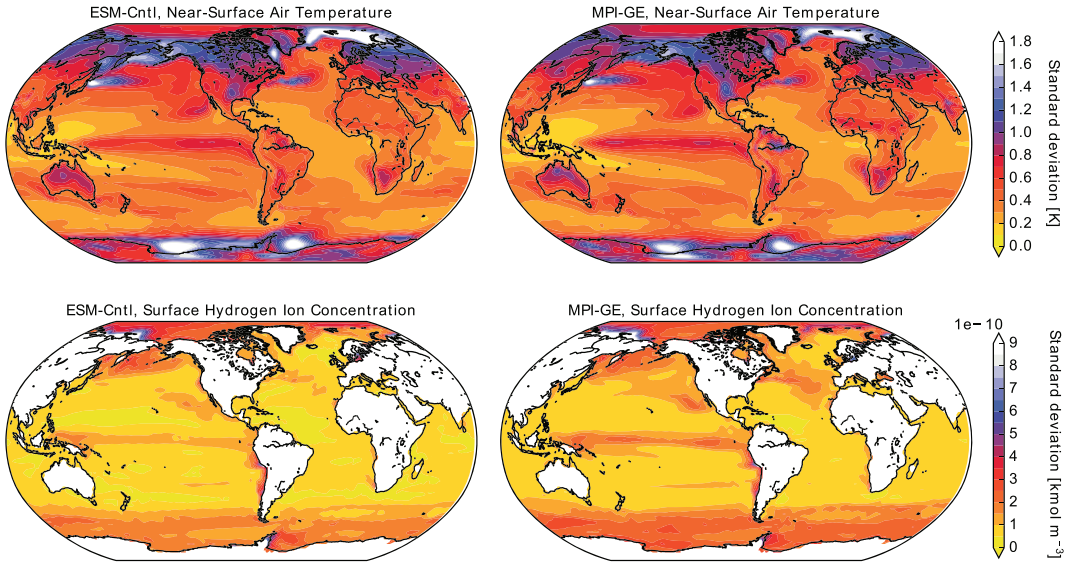

Figure A4. Standard deviation over 1,000 years of ESM-CNTRL (left panels) and over 100 ensemble members of MPI-GE from 1850–2100 (right panels) for temperature (upper panels) and hydrogen ion concentration (lower panels).

with respect to the 1,000-year mean (left panels) or to the 100-ensemble mean from 1850 to 2100 (right panels). In general, the differences in both magnitude and distribution of variability between MPI-GE and ESM-CNTL are small.

Data Availability Statement

Computational resources were made available by the German Climate Computing Center (DKRZ) through support from the German Federal Ministry of Education and Research (BMBF). Primary data are available through González and Ilyina (2016) and Sonntag et al. (2018), and scripts needed to reproduce this analysis are archived by the Max Planck Institute for Meteorology and will be available by contacting publications@mpimet.mpg.de website.

Acknowledgments
We thank A. Ribes for sharing the ROF code and A. Winkler for translating the code to python, which can be downloaded online (https://github.com/pinplex/PyDnA). We acknowledge D. Putrahasan, J. Marotzke, and one anonymous reviewer for constructive feedback on this manuscript. This research was supported by the German Science Foundation (DFG) within the Priority Program Climate Engineering: Risks, Challenges, Opportunities (SPP 1689). Open access funding enabled and organized by Projekt DEAL.

References

Allen, M. R., & Stott, P. A. (2003). Estimating signal amplitudes in optimal fingerprinting, part I: Theory. *Climate Dynamics*, *21*(5), 477–491. https://doi.org/10.1007/s00382-003-0313-9

Allen, M. R., & Tett, S. F. B. (1999). Checking for model consistency in optimal fingerprinting. *Climate Dynamics*, *15*(6), 419–434. https://doi.org/10.1007/s003820050291

Bindoff, N. L., Stott, P. A., Rao, K. M. A., Allen, M. R., Gillett, N., Gutzler, D., et al. (2013). Climate change 2013: The physical science basis. In T. F. Stocker, D. Qin, G.-K. Plattner, M. Tignor, S. K. Allen, J. Boschung, et al. (Eds.), *Contribution of working group I to the fifth assessment report of the intergovernmental panel on climate change*. Cambridge, United Kingdom and New York, NY, USA: Cambridge University Press.

Bürger, G., & Cubasch, U. (2015). The detectability of climate engineering. *Journal of Geophysical Research: Atmospheres*, *120*, 11,404–11,418. https://doi.org/10.1002/2015JD023954

Caldeira, K., Bala, G., & Cao, L. (2013). The science of geoengineering. *Annual Review of Earth and Planetary Sciences*, *41*(1), 231–256. https://doi.org/10.1146/annurev-earth-042711-105548

Crutzen, P. J. (2006). Albedo enhancement by stratospheric sulfur injections: A contribution to resolve a policy dilemma? *Climatic Change*, *77*(3), 211. https://doi.org/10.1007/s10584-006-9101-y

Dagon, K., & Schrag, D. P. (2017). Regional climate variability under model simulations of solar geoengineering. *Journal of Geophysical Research: Atmospheres*, *122*, 12,106–12,121. https://doi.org/10.1002/2017JD027110

Deser, C., Alexander, M. A., Xie, S.-P., & Phillips, A. S. (2010). Sea surface temperature variability: Patterns and mechanisms. *Annual Review of Marine Science*, *2*(1), 115–143. https://doi.org/10.1146/annurev-marine-120408-151453

Deser, C., Terray, L., & Phillips, A. S. (2016). Forced and internal components of winter air temperature trends over North America during the past 50 years: Mechanisms and implications. *Journal of Climate*, *29*(6), 2237–2258. https://doi.org/10.1175/JCLI-D-15-0304.1

Doney, S. C., Fabry, V. J., Feely, R. A., & Kleypas, J. A. (2009). Ocean acidification: The other CO_2 problem. *Annual Review of Marine Science*, *1*, 169–192.

Drijfhout, S., Hazeleger, W., Selten, F., & Haarsma, R. (2008). Future changes in internal variability of the Atlantic Meridional Overturning Circulation. *Climate Dynamics*, *30*(4), 407–419. https://doi.org/10.1007/s00382-007-0297-y

Fischer, E. M., & Schär, C. (2008). Future changes in daily summer temperature variability: Driving processes and role for temperature extremes. *Climate Dynamics*, *33*(7), 917. https://doi.org/10.1007/s00382-008-0473-8

Friedrich, T., Timmermann, A., Abe-Ouchi, A., Bates, N. R., Chikamoto, M. O., Church, M. J., et al. (2012). Detecting regional anthropogenic trends in ocean acidification against natural variability. *Nature Climate Change*, *2*, 167. https://doi.org/10.1038/nclimate1372

Frölicher, T. L., Rodgers, K. B., Stock, C. A., & Cheung, W. W. L. (2016). Sources of uncertainties in 21st century projections of potential ocean ecosystem stressors. *Global Biogeochemical Cycles*, *30*, 1224–1243. https://doi.org/10.1002/2015GB005338

Frölicher, T. L., Sarmiento, J. L., Paynter, D. J., Dunne, J. P., Krasting, J. P., & Winton, M. (2015). Dominance of the southern ocean in anthropogenic carbon and heat uptake in CMIP5 models. *Journal of Climate*, *28*(2), 862–886. https://doi.org/10.1175/JCLI-D-14-00117.1

Fuss, S., Canadell, J. G., Peters, G. P., Tavoni, M., Andrew, R. M., Ciais, P., et al. (2014). Betting on negative emissions. *Nature Climate Change*, *4*, 850–853. https://doi.org/10.1038/nclimate2392

Gabriel, C. J., & Robock, A. (2015). Stratospheric geoengineering impacts on El Niño/Southern Oscillation. *Atmospheric Chemistry and Physics*, *15*(20), 11,949–11,966. https://doi.org/10.5194/acp-15-11949-2015

Giorgetta, M. A., Jungclaus, J., Reick, C. H., Legutke, S., Bader, J., Bttinger, M., et al. (2013). Climate and carbon cycle changes from 1850 to 2100 in MPI-ESM simulations for the coupled model intercomparison project phase 5. *Journal of Advances in Modeling Earth Systems*, *5*, 572–597. https://doi.org/10.1002/jame.20038

Goll, D., Brovkin, V., Liski, J., Raddatz, T., Thum, T., & Todd-Brown, K. (2015). Strong dependence of CO_2 emissions from anthropogenic land cover change on soil carbon parametrization and initial land cover. *Global Biogeochemical Cycles*, *29*, 1–58.

González, M. F., & Ilyina, T. (2016). Impacts of artificial ocean alkalinization on the carbon cycle and climate in Earth system simulations. *Geophysical Research Letters*, *43*, 6493–6502. https://doi.org/10.1002/2016GL068576

González, M. F., Ilyina, T., Sonntag, S., & Schmidt, H. (2018). Enhanced rates of regional warming and ocean acidification after termination of large scale ocean alkalinization. *Geophysical Research Letters*, *45*, 7120–7129. https://doi.org/10.1029/2018GL077847

Hagemann S., & Stacke, T. (2015). Impact of the soil hydrology scheme on simulated soil moisture memory. *Climate Dynamics*, *44*(7), 1731–1750. https://doi.org/10.1007/s00382-014-2221-6

Hartmann, J., West, A. J., Renforth, P., Khler, P., De La Rocha, C. L., Wolf-Gladrow, D. A., et al. (2013). Enhanced chemical weathering as a geoengineering strategy to reduce atmospheric carbon dioxide, supply nutrients, and mitigate ocean acidification. *Reviews of Geophysics*, *51*, 113–149. https://doi.org/10.1002/rog.20004

Hasselmann, K. (1993). Optimal fingerprints for the detection of time-dependent climate change. *Journal of Climate*, *6*(10), 1957–1971. https://doi.org/10.1175/1520-0442(1993)006<1957:OFFTDO>2.0.CO;2

Hausfather, Z., & Peters, G. P. (2020). Emissions the 'business as usual' story is misleading. *Nature*, *577*(618-620). https://doi.org/10.1007/s003820050186

Hegerl, G. C., Hasselmann, K., Cubasch, U., Mitchell, J. F. B., Roeckner, E., Voss, R., & Waszkewitz, J. (1997). Multi-fingerprint detection and attribution analysis of greenhouse gas, greenhouse gas-plus-aerosol and solar forced climate change. *Climate Dynamics*, *13*(9), 613–634. https://doi.org/10.1007/s003820050186

Hegerl, G. C., & Zwiers, F. (2011). Use of models in detection and attribution of climate change. *Wiley Interdisciplinary Reviews: Climate Change*, *2*, 570–591. https://doi.org/10.1002/wcc.121

IPCC (2018). Annex I: Glossary. Global Warming of 1.5 C. An IPCC Special Report on the impacts of global warming of 1.5 C above pre-industrial levels and related global greenhouse gas emission pathways, in the context of strengthening the global response to the threat of climate change, sustainable development, and efforts to eradicate poverty, In Press.

Ilyina, T., Six, K. D., Segschneider, J., Maier-Reimer, E., Li, H., & Nez-Riboni, I. (2013). Global ocean biogeochemistry model HAMOCC: Model architecture and performance as component of the MPI-Earth system model in different CMIP5 experimental realizations. *Journal of Advances in Modeling Earth Systems*, *5*, 287–315. https://doi.org/10.1029/2012MS000178

Irvine, P. J., Kravitz, B., Lawrence, M. G., & Muri, H. (2016). An overview of the earth system science of solar geoengineering. *Wiley Interdisciplinary Reviews: Climate Change*, *7*(6), 815–833. https://doi.org/10.1002/wcc.423

Jungclaus, J. H., Fischer, N., Haak, H., Lohmann, K., Marotzke, J., Matei, D., et al. (2013). Characteristics of the ocean simulations in the Max Planck Institute Ocean Model (MPIOM) the ocean component of the MPI-Earth system model. *Journal of Advances in Modeling Earth Systems*, *5*, 422–446. https://doi.org/10.1002/jame.20023

Knutti, R., Masson, D., & Gettelman, A. (2013). Climate model genealogy: Generation CMIP5 and how we got there. *Geophysical Research Letters*, *40*, 1194–1199. https://doi.org/10.1002/grl.50256

Kravitz, B., Robock, A., Boucher, O., Schmidt, H., Taylor, K. E., Stenchikov, G., & Schulz, M. (2011). The geoengineering model intercomparison project (geomip). *Atmospheric Science Letters*, *12*(2), 162–167. https://doi.org/10.1002/asl.316

Lawrence, M. G., Schfer, S., Muri, H., Scott, V., Oschlies, A., Vaughan, N. E., et al. (2018). Evaluating climate geoengineering proposals in the context of the Paris Agreement temperature goals. *Nature Communications*, *1*, 3734. https://doi.org/10.1038/s41467-018-05938-3

Lo, Y. T. E., Charlton-Perez, A. J., Highwood, E. J., & Lott, F. C. (2018). Best scale for detecting the effects of stratospheric sulfate aerosol geoengineering on surface temperature. *Earth's Future*, *6*(12), 1660–1671. https://doi.org/10.1029/2018EF000933

Lo, Y. T. E., Charlton-Perez, A. J., Lott, F. C., & Highwood, E. J. (2016). Detecting sulphate aerosol geoengineering with different methods. *Scientific Reports*, *6*, 39,169. https://doi.org/10.1038/srep39169

Lovenduski, N. S., Long, M. C., & Lindsay, K. (2015). Natural variability in the surface ocean carbonate ion concentration. *Biogeosciences*, *12*(21), 6321–6335. https://doi.org/10.5194/bg-12-6321-2015

Maher, N., Milinski, S., Suarez-Gutierrez, L., Botzet, M., Dobrynin, M., Kornblueh, L., et al. (2019). The Max Planck institute grand ensemble—Enabling the exploration of climate system variability. *Journal of Advances in Modeling Earth Systems*, *11*, 2050–2069. https://doi.org/10.1029/2019MS001639

Meehl, G. A., Washington, W. M., Wigley, T. M. L., Arblaster, J. M., & Dai, A. (2003). Solar and greenhouse gas forcing and climate response in the twentieth century. *Journal of Climate*, *16*(3), 426–444. https://doi.org/10.1175/1520-0442(2003)016<0426:SAGGFA>2.0.CO;2

Modak, A., Bala, G., Cao, L., & Caldeira, K. (2016). Why must a solar forcing be larger than a CO_2 forcing to cause the same global mean surface temperature change? *Environmental Research Letters*, *11*(4), 044013. https://doi.org/10.1088/1748-9326/11/4/044013

Niemeier, U., Schmidt, H., Alterskjær, K., & Kristjánsson, J. E. (2013). Solar irradiance reduction via climate engineering: Impact of different techniques on the energy balance and the hydrological cycle. *Journal of Geophysical Research: Atmospheres*, *118*, 11,905–11,917. https://doi.org/10.1002/2013JD020445

Niemeier, U., & Timmreck, C. (2015). What is the limit of climate engineering by stratospheric injection of SO_2? *Atmospheric Chemistry and Physics*, *15*(16), 9129–9141. https://doi.org/10.5194/795acp-15-9129-2015

Olonscheck, D., & Notz, D. (2017). Consistently estimating internal climate variability from climate model simulations. *Journal of Climate*, *30*(23), 9555–9573. https://doi.org/10.1175/JCLI-D-16-0428.1

Oschlies, A., Held, H., Keller, D., Keller, K., Mengis, N., Quaas, M., et al. (2017). Indicators and metrics for the assessment of climate engineering. *Earth's Future*, *5*, 49–58. https://doi.org/10.1002/2016EF000449

Pendergrass, A. G., Knutti, R., Lehner, F., Deser, C., & Sanderson, B. M. (2017). Precipitation variability increases in a warmer climate. *Scientific Reports*, *7*(1), 17,966. https://doi.org/10.1038/s41598-017-17966-y

Pfrommer, T., Goeschl, T., Proelss, A., Carrier, M., Lenhard, J., Martin, H., et al. (2019). Establishing causation in climate litigation: Admissibility and reliability. *Climatic Change*, *152*(1), 67–84. https://doi.org/10.1007/s10584-018-2362-4

Reick, C. H., Raddatz, T., Brovkin, V., & Gayler, V. (2013). Representation of natural and anthropogenic land cover change in MPI-ESM. *Journal of Advances in Modeling Earth Systems*, *5*, 459–482. https://doi.org/10.1002/jame.20022

Ribes, A., Azaïs, J.-M., & Planton, S. (2009). Adaptation of the optimal fingerprint method for climate change detection using a well-conditioned covariance matrix estimate. *Climate Dynamics*, *33*(5), 707–722. https://doi.org/10.1007/s00382-009-0561-4

Ribes, A., Planton, S., & Terray, L. (2013). Application of regularised optimal fingerprinting to attribution. Part I: Method, properties and idealised analysis. *Climate Dynamics*, *41*(11), 2817–2836. https://doi.org/10.1007/s00382-013-1735-7

Ribes, A., & Terray, L. (2013). Application of regularised optimal fingerprinting to attribution. Part II: Application to global near-surface temperature. *Climate Dynamics*, *41*(11), 2837–2853. https://doi.org/10.1007/s00382-013-1736-6

Ribes, A., Zwiers, F. W., Azaïs, J.-M., & Naveau, P. (2017). A new statistical approach to climate change detection and attribution. *Climate Dynamics*, *48*(1), 367–386. https://doi.org/10.1007/s00382-016-3079-6

Rogelj, J., den Elzen, M., Höhne, N., Fransen, T., Fekete, H., Winkler, H., et al. (2016). Paris agreement climate proposals need a boost to keep warming well below 2 °C. *Nature*, *534*, 631–639. https://doi.org/10.1038/nature18307

Royal Society (2009). Geoengineering the climate: Science, governance and uncertainty. Royal Society Policy Document 10/09, http://royalsociety.org/policy/publications/2009/geoengineering-climate

Schlunegger, S., Rodgers, K. B., Sarmiento, J. L., Frölicher, T. L., Dunne, J. P., Ishii, M., & Slater, R. (2019). Emergence of anthropogenic signals in the ocean carbon cycle. *Nature Climate Change*, *9*(9), 719–725. https://doi.org/10.1038/s41558-019-0553-2

Sippel, S., Meinshausen, N., Merrifield, A., Lehner, F., Pendergrass, A. G., Fischer, E., & Knutti, R. (2019). Uncovering the forced climate response from a single ensemble member using statistical learning. *Journal of Climate*, *32*(17), 5677–5699. https://doi.org/10.1175/JCLI-D-18-0882.1

Sonntag, S., Ferrer González, M., Ilyina, T., Kracher, D., Nabel, J. E. M. S., Niemeier, U., et al. (2018). Quantifying and comparing effects of climate engineering methods on the Earth system. *Earth's Future*, *6*(2), 149–168. https://doi.org/10.1002/2017EF000620

Stevens, B., Giorgetta, M., Esch, M., Mauritsen, T., Crueger, T., Rast, S., et al. (2013). Atmospheric component of the MPM Earth System Model: ECHAM6. *Journal of Advances in Modeling Earth Systems*, *5*, 146–172. https://doi.org/10.1002/jame.20015

Stott, P. A. (2003). Attribution of regional-scale temperature changes to anthropogenic and natural causes. *Geophysical Research Letters*, *30*(14), 1724.

Tavoni, M., & Socolow, R. (2013). Modeling meets science and technology: An introduction to a special issue on negative emissions. *Climatic Change*, *118*(1), 1–14. https://doi.org/10.1007/s10584-013-0757-9

Taylor, K. E., Stouffer, R. J., & Meehl, G. A. (2012). An overview of CMIP5 and the experiment design. *Bulletin of the American Meterological Society*, *93*, 485–498. https://doi.org/10.1175/BAMS-D-11-00094.1

Thomas, J., Waugh, D., & Gnanadesikan, A. (2018). Relationship between ocean carbon and heat multidecadal variability. *Journal of Climate*, *31*(4), 1467–1482. https://doi.org/10.1175/JCLI-D-17-0134.1

UNFCCC (2015). Adoption of the Paris agreement. 21st Conference of the Parties, Paris: United Nations.

Vaughan, N. E., & Lenton, T. M. (2012). Interactions between reducing CO_2 emissions, CO_2 removal and solar radiation management. *Philosophical Transactions of the Royal Society A: Mathematical, Physical and Engineering Sciences*, *370*(1974), 4343–4364. https://doi.org/10.1098/rsta.2012.0188

Zhao, A., Stevenson, D. S., & Bollasina, M. A. (2019). Climate forcing and response to greenhouse gases, aerosols, and ozone in CESM1. *Journal of Geophysical Research: Atmospheres*, *124*, 13,876–13,894. https://doi.org/10.1029/2019JD030769

Zürn, M., & Schäfer, S. (2013). The paradox of climate engineering. *Global Policy*, *4*(3), 266–277. https://doi.org/10.1111/gpol.12004